

Single-shot complete spatiotemporal measurement of terawatt laser pulses

Elizabeth Grace^{1,2,*} , Tammy Ma² , Zhe Guang¹ , Rana Jafari¹ , Jaebum Park³ , Jerry Clark^{2,4} , Gregory Kemp² , James Moody² , Michelle Rhodes² , Yuan Ping² , Ronnie Shepherd² , Brent Stuart²  and Rick Trebino¹ 

¹ School of Physics, Georgia Institute of Technology, Atlanta, GA, United States of America

² Lawrence Livermore National Laboratory, Livermore, CA, United States of America

³ Electrical and Computer Engineering, Colorado State University, Fort Collins, CO, United States of America

⁴ Physics Department, Florida A&M University, Tallahassee, FL, United States of America

E-mail: esgrace@gatech.edu

Received 4 March 2021, revised 20 May 2021

Accepted for publication 15 June 2021

Published 13 July 2021



Abstract

We demonstrate, for the first time, a single-shot, complete spatiotemporal measurement of pulses from a terawatt-scale, multi-stage-amplified, low repetition-rate laser source. The ultrashort pulse electric field, $E(x,y,z,t)$, is spatiotemporally complex due to distortions that accrue from multiple chirped-pulse amplifiers, which requires a complete characterization. Meanwhile, the instability of the laser source introduces field profiles that vary significantly from pulse to pulse, which, together with the low repetition-rate (15 shots/hour), requires the use of a single-shot measurement technique. To accomplish the measurements, we used a wavelength-multiplexed, digital-holographic technique called Spatially and Temporally Resolved Intensity and Phase Evaluation Device: Full Information from a Single Hologram, specially tailored to measure picosecond pulses at a wavelength of about 1 μm . Specifically, individual pulses from the compact multipulse terawatt laser were measured, with up to 0.3 J per shot of energy and ~ 2 ps pulse durations, at 1052 nm. With these measurements, we characterized several major spatiotemporal distortions that affect the peak intensity at the laser focus, as well as the pulse-shape instability on a shot-to-shot basis. Our technique allows detailed diagnosis of laser pulses (especially high-order spatiotemporal distortions) and provides straightforward four-dimensional animations of pulse propagation to a focus.

Keywords: holography, pulse, measurement

(Some figures may appear in colour only in the online journal)

1. Introduction

A high-intensity laser pulse's interaction with matter at or near a focus depends sensitively on the pulse's intensity and phase, and unexpected and undesirable behavior can result from distortions in the pulse [1, 2]. Unfortunately, high-intensity laser systems often suffer from temporal artifacts such as satellite pulses and pre-pulse pedestals [3, 4]. In addition, distortions in the intensity and/or phase as a function of time

and space, that is, spatiotemporal distortions, can significantly decrease the focal-spot peak intensity. Such distortions, in which the pulse's temporal intensity and phase vary with transverse position, can arise from misalignment, optical aberrations, and intensity-induced coupling effects. Common simple first-order spatiotemporal distortions include well-known distortions, like angular dispersion, spatial chirp, and pulse-front tilt, as well as more exotic distortions such as wave-front rotation and the ultrafast lighthouse effect [5]. But significantly more complex spatiotemporal distortions also commonly occur, and the resulting pulse can be highly complex [6]. Worse, the regenerative-amplification process in a

* Author to whom any correspondence should be addressed.

chirped-pulse amplifier can easily magnify spatiotemporal distortions in the pulse, which in the end lead to significantly diminished focal-spot intensity [7–11]. This is especially true with multi-stage-amplified, Terawatt-scale laser sources, such as the COmpact MultipulsE Terawatt (COMET) laser at the Jupiter Laser Facility [12, 13], where long-pulse (2 ns) and short-pulse (0.5–100 ps) configurations are cascaded concurrently to achieve pulse energies up to 12 J on target. Tremendous effort is required to maintain such lasers at the highest output intensity and with a relatively well-defined temporal duration and an aberration-free focal spot.

Unfortunately, even in the presence of simple first-order spatiotemporal couplings, any diagnostic that measures time-averaged or space-averaged quantities cannot fully reveal the pulse. As a result, a complete spatiotemporal intensity-and-phase pulse-measurement technique, that is, one that does not involve such temporal or spatial averaging, is required to both understand and optimize such pulses.

To further complicate the measurement, high-intensity laser sources necessarily have low repetition rates—as low as one shot per day [14]—rendering multi-shot methods impractical. Furthermore, such low rep rates (coupled with the pulses' high power) mean that the output pulses can also suffer from severe shot-to-shot pulse instability, necessitating single-shot measurement of the complete spatiotemporal intensity and phase of such pulses. This is a much more challenging task [15]. Shot-to-shot fluctuations in the simple peak intensity, when reported, typically have rather high values of 10%–20% [16]. Shot-to-shot variations in the spatially averaged pulse temporal intensity and phase can be measured using single-shot pulse- temporal-intensity-and-phase measurement methods, such as the popular GRENOUILLE technique [17–24]. GRENOUILLE also measures the first-order spatiotemporal distortions on a single shot [25, 26]. But more complex spatiotemporal distortions occur in high-power pulses, and their variations from shot to shot and their resulting effects have remained largely immeasurable [27] and can contaminate experimental data and lead to mistaken conclusions. For instance, laser-driven ion acceleration depends on the driving optical pulse's spatial and temporal shape [28], and instability can introduce severe smearing effects.

Most pulse-characterization techniques, especially spatiotemporal ones, must scan a parameter, such as a pulse delay, and so necessarily must average over many pulses. As a result, previous methods used to measure such spatiotemporal distortions in high-intensity laser pulses have required averaging over multiple shots, thus missing any pulse-to-pulse variations [29–37]. Indeed, to our knowledge, no single-shot complete spatiotemporal intensity-and-phase measurement has ever been made of a high-intensity pulse.

To solve this problem, we have developed a single-shot complete-spatiotemporal intensity-and-phase pulse-measurement technique, Spatially and Temporally Resolved Intensity and Phase Evaluation Device: Full Information from a Single Hologram, or STRIPED FISH [38–43], which measures $E(x, y, \omega)$ on a single shot. From this measurement, simple Fourier transformation and a diffraction integral then directly yield $E(x, y, z, t)$. STRIPED FISH is designed to measure a

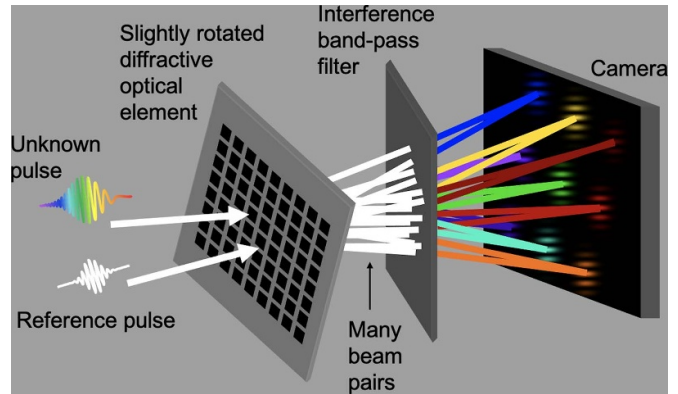


Figure 1. Schematic of STRIPED FISH device. The unknown and reference beams cross at the slightly rotated 2D DOE, producing many beam pairs at different angles which impinge upon an ultranarrow IBPF. The resulting wavelength-multiplexed holograms are then imaged onto the camera sensor.

nearly collimated beam, but this last step allows a STRIPED FISH measurement made away from a focus to provide the complete field at a focus as well.

Previously, we have used STRIPED FISH to rapidly measure trains of spatiotemporally complex pulses using only a single camera frame [40–44]. The measurements reported here are, to our knowledge, the first true single-shot complete spatiotemporal intensity-and-phase measurements ever reported for any pulse.

2. Working principles of STRIPED FISH

STRIPED FISH simultaneously generates multiple holograms of the unknown pulse, all of different wavelengths. To accomplish this, the unknown pulse and a completely characterized reference pulse first cross at a small angle in the vertical plane (see figure 1). Next, a 2D diffractive optical element (DOE) transforms them into an array of vertically crossed beam pairs, each at a unique horizontal propagation angle. It should be noted here that the DOE is chosen to have negligible angular dispersion within all the various diffraction orders detected by the STRIPED FISH camera and so only functions to replicate the original beam pair. Finally, for each beam pair, an interference bandpass filter (IBPF) then transmits a very narrow range of wavelengths, each determined entirely by the beam pair's horizontal incidence angle. The result is an array of quasi-monochromatic holograms.

Note that, in order to achieve holograms, all of different wavelengths, the DOE is rotated slightly about the system optic axis, yielding a tilted array of beam pairs, each of whose horizontal incidence angles at the bandpass filter is different. Also, to obtain a completely characterized reference pulse, some of the unknown beam is split off before the STRIPED FISH device, spatially filtered to achieve a smooth spatial profile free of spatiotemporal distortions, and temporally characterized by GRENOUILLE [17]. In addition to its role in generating the holograms and, after the fact, deconvolving each frequency's spatial field from its hologram (see below), the reference pulse's spectral phase also provides the relative phases

of the various fields derived from each hologram. In addition, the beam pairs pass through a lens that serves to image their input plane onto the camera sensor, where they cross and interfere, producing the required spatial fringes. All the holograms are measured simultaneously on a single camera frame.

We note here that for single-shot measurements, such as STRIPED FISH, interferometric stability is not relevant to either the reference-pulse or unknown-pulse measurement. Because we measure one pulse at a time, we can actually watch the fringes possibly vary from shot to shot, indicating interesting variations that would pose a problem for multi-shot measurements.

As alluded to above, because the reference pulse is spatiotemporally known, the unknown pulse's field at each frequency can be extracted from its spatial fringes according to the basic equation of holography:

$$I(x, y, \omega) = |E_{\text{unk}}(x, y, \omega)|^2 + |E_{\text{ref}}(x, y, \omega)|^2 + E_{\text{unk}}(x, y, \omega) E_{\text{ref}}^*(x, y, \omega) e^{ik \sin(\alpha)} + E_{\text{ref}}(x, y, \omega) E_{\text{unk}}^*(x, y, \omega) e^{-ik \sin(\alpha)} \quad (1)$$

where E_{unk} is the unknown pulse to be measured, E_{ref} is the known reference pulse, and α is the crossing angle between the two beams. This intensity profile can be thought of as a sum of slowly varying (the first two) and rapidly varying (the last two) terms. The slowly varying terms are Fourier-filtered out, and just one of the rapidly varying terms is kept. This term provides the full intensity and phase information vs. x and y , corresponding to its frequency, $E(x, y, \omega)$, relative to that of the reference pulse. The complete field information is extracted using the STRIPED FISH pulse-retrieval algorithm, which combines the retrieved x – y field profiles, $E(x, y, \omega)$, for each frequency ω found from each hologram [27]. Combining them together using the relative spectral phase information from the reference pulse produces the pulse field vs. two spatial dimensions and frequency, $E_{\text{unk}}(x, y, \omega)$. This information is sufficient to reconstruct the entire spatiotemporal pulse field (except for the single parameter of an irrelevant overall constant phase), and the remaining pulse field dependence on z is obtained from diffraction integrals [45]. The pulse's temporal dependence can be found simply by inverse-Fourier-transforming this result from frequency to time. The result of a STRIPED FISH measurement is a complete spatiotemporal measurement from a single camera frame [38–44].

3. Implementation and measurement of terawatt laser pulses

The STRIPED FISH device used in this experiment was designed and built specifically for the COMET laser system (see figure 2). This device's DOE is a photomask printed on soda lime glass with anti-reflective chrome coating that is periodic in both transverse directions. The period and critical dimension of the DOE were selected so that the spectrum would be sampled with better resolution than that of the IBPF. In particular, a square hole size of $11 \mu\text{m}$ with a pitch of $55 \mu\text{m}$

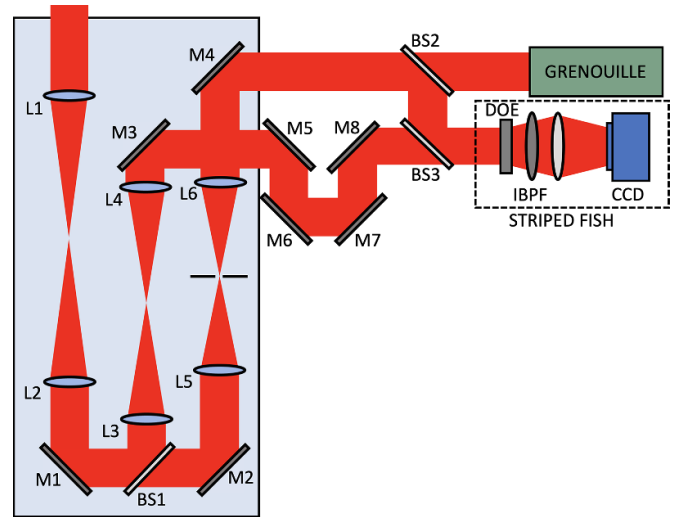


Figure 2. Experimental setup for pulse measurement of pulses emitted by COMET at the JLF, including the chamber setup and STRIPED FISH pickoff. The beam enters the vacuum chamber and is down-collimated through lenses L1 ($f = 1000 \text{ mm}$) and L2 ($f = 150 \text{ mm}$) before it is split into the unknown and reference beam arms by beam-splitter BS1 (90/10). The unknown beam arm uses L3 and L4 ($f = 400 \text{ mm}$) to relay image a point in the chamber to the diffraction grating (DOE) of STRIPED FISH. The reference beam enters a spatial filter with a 32 micron pinhole at the focus of lens L5 ($f = 200 \text{ mm}$), which is then magnified after lens L6 ($f = 500 \text{ mm}$). A pickoff transmits the spatially filtered reference pulse to a Swamp Optics GRENOUILLE at BS2 (50/50) and reflects the reference pulse to be recombined with the unknown pulse at BS3 (50/50) before entering STRIPED FISH.

was used; this ratio of 5:1 produces four subsidiary maxima on each side of the zeroth order, corresponding to a 9×9 grid and a maximum angle of incidence (AOI) of 4.4 degrees on the IBPF. This maximum AOI was chosen to match the IBPF's center wavelength vs. AOI curves, which were provided by the manufacturer.

The temporal range of STRIPED FISH depends mainly on the filter bandwidth [43]. The ultranarrow IBPF in the COMET setup has a pass band of 0.1 nm, which spreads when tilted to 0.3 nm, and the resulting temporal range for this device is 12.3 ps. The STRIPED FISH device was implemented at COMET using the setup shown in figure 2.

The COMET laser is a tabletop chirped-pulse-amplified laser system at the Jupiter Laser Facility that was recently rebuilt at the time of measurement. The system has four beam configurations, able to run concurrently, with pulse lengths from 1 ps to 2 ns and beam energies up to 20 J. This work was performed using the compressed-short pulse configuration, which has an available pulse length range of 0.5–100 ps at 1ω and a repetition rate of 15 shots/hour. The COMET laser consists of a Nd:glass oscillator and a Ti:sapphire regenerative amplifier tuned to 1052 nm with a four-stage Nd:phosphate glass amplifier section. The 200 fs oscillator pulse is stretched to 750 ps with the folded single-grating pulse stretcher, then amplified to 5 mJ in the regenerative amplifier. The pulse is passed through three successive rod amplifiers with diameters

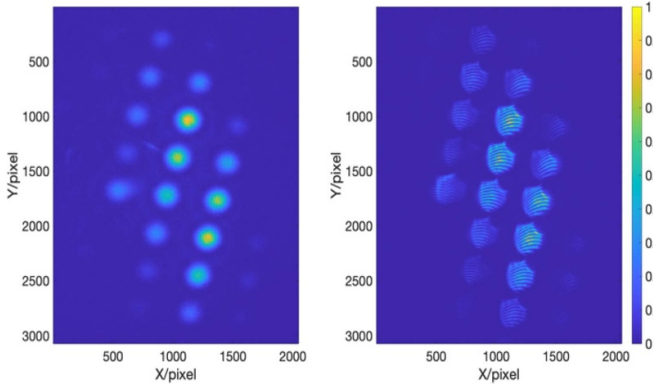


Figure 3. STRIPED FISH trace with the reference pulse alone (left) and data trace with both beams present (right) for a representative fully amplified shot. The number of holograms is chosen so that the spectrum is sampled with a better resolution than that of the IBPF (see figure 1).

of 7 mm, 16 mm, and 25 mm. In normal operation, the beam would then double-pass a 50 mm rod amplifier ($G = 10$), but this component was unavailable at the time of measurement. The beam is then sent to the vacuum grating-compressor box, which contains two double-passed gratings.

STRIPED FISH measurements were taken on the COMET laser at two amplification conditions: maximum and partial. The maximum amplification condition, which had an average energy of 300 mJ, used all three available amplifiers, while the partial amplification condition had an average energy of 30 mJ and charged only the first and last amplifiers. A wave plate between crossed polarizers after the last amplifier was used to attenuate the delivered energy to the diagnostic. Twenty-two data shots were taken at maximum amplification, and just five data shots were taken at partial amplification. Data and reference STRIPED FISH traces for one such fully amplified shot are shown in figure 3.

4. Retrieval of the complete spatiotemporal electric field

The set of complete spatiotemporal electric fields corresponding to each shot's data trace is retrieved using the STRIPED FISH retrieval algorithm [40], with one key improvement made. The single-shot STRIPED FISH algorithm uses the quickly varying term (see equation (1)) from the data trace (see figure 3) along with the full spatio-spectral field of the reference pulse, which is acquired from the GRENOUILLE measurement and the reference frame, for retrieving both the intensity and phase information of the unknown pulse. The calibration for the relative intensities of the holograms in the data trace is obtained by using the spectrum of the reference pulse and the reference frame (see figure 3). In addition, the newly developed RANA retrieval algorithm for SHG traces is used to retrieve the reference pulse's intensity and phase from the GRENOUILLE trace [46].

During the retrieval analysis, corner suppression is applied by multiplying each hologram by a radially symmetric super-Gaussian of order 10, which forces the values at the perimeter, and especially at the corners, to zero. Low-pass Fourier-filtering is implemented by 2D Fourier transforming each hologram, multiplying the transformed hologram by a top-hat function, and inverse 2D Fourier transforming the result back to image space. A top-hat function of radius equal to $\sigma N/2$ pixels, where $N = 100$ is the number of pixels in x and y for each hologram and $\sigma = 0.4$, is used. The effect of low-pass filtering is to remove the higher spatial frequencies corresponding to noise [47].

5. Discussion and interpretation of systematic results

It is worth reiterating that, as mentioned earlier, STRIPED FISH is unique in its ability to measure highly complex pulses in space and time with no assumptions about the pulse or beam [38, 39], and to do so on a single shot. As a result, it can quantify the higher-order spatiotemporal dependencies (and any other distortions) on a single shot.

Across all shots in our experiment, the linear and higher-order spatiotemporal distortions generally show systematic behavior, but with some variations from shot to shot. In our measurements, the average pulse length is 2.4 ± 0.09 ps.

The trends in spatiotemporal distortions across all measurements are most intuitively seen in the intensity plots captured in figure 4, which show the spatiotemporal dependencies in the x direction integrated over all shots. The pulse front tilt (figure 4(a)), spatial chirp (figure 4(b)), ultrafast lighthouse effect (figure 4(c)) and angular dispersion (figure 4(d)) are all present, as seen by the nonzero slope in the relevant domains [41]. Pulse front tilt and spatial chirp are well-studied consequences of angular dispersion [48, 49], which can emerge from angularly dispersive elements, including diffraction gratings in a CPA laser [7, 50–52]. Due to the mathematical interdependence of the spatiotemporal distortions [5], the ultrafast lighthouse effect (angle-time coupling) is also present.

To assess the severity of measured first-order spatiotemporal distortions, a normalized correlation parameter ρ was previously defined for each of the four intensity couplings in figure 4 [53]. For instance, the correlation coefficient for pulse front tilt is

$$\rho_{xt} = \frac{\iint dx dt I(x, t) xt}{\Delta x \Delta t},$$

$$\text{where } \Delta x = \left[\iint dx dt I(x, t) x^2 \right]^{1/2}, \quad (2)$$

$$\text{and } \Delta t = \left[\iint dx dt I(x, t) t^2 \right]^{1/2}.$$

The correlation coefficients for the remaining first order distortions are analogously defined. This parameter was designed as an intuitive metric to quantify the amount of distortion in any arbitrary given pulse on a scale from -1

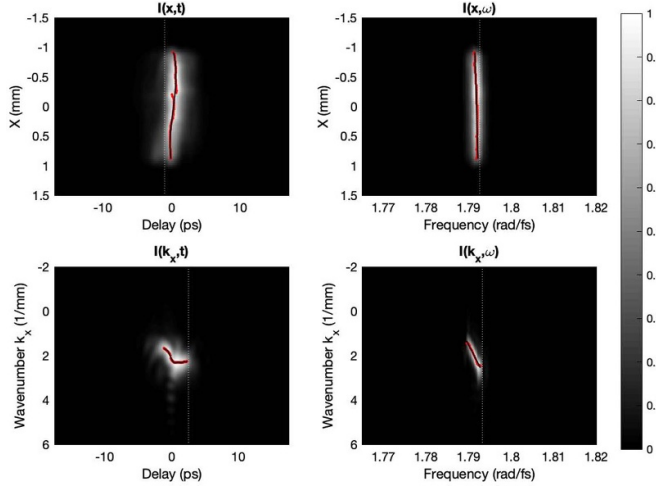


Figure 4. Pulse intensities along the x direction in the spatiotemporal and spatio-spectral domains averaged over all shots. In each frame, the maxima of the images are plotted in red, with the polynomial of best fit plotted in black. A dotted vertical reference line is plotted in white. (a) Pulse intensity summed over y in the spatiotemporal domain. The intensity $I(x,t)$ has linear dependence between x and t , which indicates pulse-front tilt. (b) Pulse intensity summed over y in the spatio-spectral domain. Similarly, the intensity $I(x,\omega)$, shows dependence between x and ω , indicating spatial chirp. (c) Pulse intensity summed over k_y in the wavenumber-time domain. The field intensity $I(k_x,t)$ shows the presence of the ultrafast lighthouse effect. (d) Pulse intensity summed over k_y in the wavenumber-frequency domain. The field intensity $I(k_x,\omega)$ has a linear dependence between k_x and ω , which indicates angular dispersion.

Table 1. Mean ρ value across all shots for all first-order amplitude couplings.

Domain	Amplitude coupling	Parameter ρ	
		x	y
(x,t)	Pulse-front tilt	−0.3	0.5
(x,ω)	Spatial chirp	0.1	−0.2
(k,t)	Lighthouse effect	0.7	−0.5
(k,ω)	Angular dispersion	0.9	−0.7

to 1, with heightened sensitivity to small levels of distortion. Generally, the magnitude of these parameters should be kept under 0.3–0.4 for optimal, quasi-Fourier-limited performance [53]. For this data, the normalized pulse-front-tilt parameter was extracted from the intensity profile integrated over all shots (see figure 4(a)). While the amount of pulse front tilt and angular dispersion are high, the amount of spatial chirp is low (see table 1), which can occur when spatial chirp but not angular dispersion is correctly compensated in a chirped pulse amplification system (analogous to the removal of the third prism in a four-prism pulse compressor) [54, 55]. We attribute the first-order angular dispersion and resulting pulse front tilt and spatial chirp to a misalignment of one of the multi-passed gratings in the pulse compressor or stretcher [48, 49].

Table 2. Mean R -squared values by polynomial order of shear fit.

Order	Pulse front tilt		Spatial chirp	
	x	y	x	y
1	0.74	0.90	0.73	0.83
2	0.78	0.93	0.91	0.88
3	0.91	0.93	0.92	0.94
4	0.91	0.99	0.93	0.98
5	0.91	0.99	0.93	0.98

To quantify the average linear spatiotemporal distortions across all shots, the shear of each integrated intensity profile (see figure 4) is extracted [25]. The angle of first order pulse front tilt is calculated from the line of best fit to the maxima of the integrated image in figure 4(a). Across all shots, the average value of the angle of first order pulse front tilt is 0.16 mrad in x and 0.30 mrad in y . From the shear of the integrated spatio-spectral image in figure 4(b), the linear spatial chirp is 0.06 mm fs in the x direction and −0.17 mm fs in the y direction.

In order to determine the contribution of nonlinear spatiotemporal distortions, the coefficient of determination R^2 is used to assess the proportion of variance in the data that is explained by linear regression to a higher-order fit [56]. To assess the nonlinear pulse front tilt, the maxima of the integrated spatiotemporal intensity image (see figure 4(a)) are fit to polynomials, resulting in the R^2 values in table 2. The R^2 value for pulse front tilt in the x direction jumped from 0.78 to 0.91 between the second and third orders and remained constant with increased orders; from this we conclude that the majority nonlinear contribution in the x -direction comes from the third-order term. Meanwhile, substantial fourth-order pulse front tilt is present in the y -direction. Higher-order pulse front tilt can be caused by higher-order angular dispersion [57]. To assess the nonlinear spatial chirp, an identical analysis was performed for the integrated spatio-spectral intensity image (see figure 4(b)). The majority nonlinear contribution is second order in the x -direction and third order in y (see table 2).

6. Shot-to-shot variations in spatiotemporal distortions

To investigate the shot-to-shot variations, we first analyze the spectral and temporal phase vs. transverse position (x and y). By the shift theorem, a linear spectral phase is a delay in arrival time, and a linear temporal phase is a shift in center frequency [5]. As a result, a change in linear spectral phase over position indicates pulse-front tilt, and the change in linear temporal phase over position gives the spatial chirp.

In figure 5, the temporal and spectral phase for a single shot is investigated along the x -direction at the points shown in figure 5(a). In figure 5(b), the spectral phase plots over x are plotted with their fits. The spectral phase peak moves to the right with x (red to blue), which indicates that the first order coefficient, which is proportional to the arrival time, is

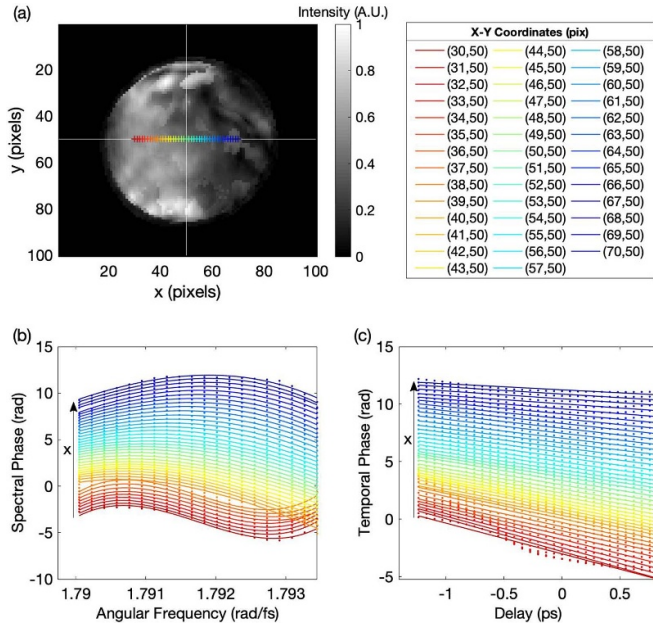


Figure 5. Phase curves along x integrated over y for shot 12 of 22 maximum energy shots. The color coding from red to blue (in the direction of the arrow) indicates the horizontal position across the beam, moving left to right. (a) Sampling coordinates, color coded and overlaid on the time-integrated spatial profile for this shot. White lines at $y = 50$ and $x = 50$ indicate the center of the beam. (b) Spectral phase curves across x . The spectral phase is cubic on the left (red) and parabolic on the right (blue). The peak of the spectral phase moves from lower to higher angular frequencies across the beam's horizontal axis (indicated with an arrow). (c) Temporal phase curves across x . The temporal phase remains roughly linear at all positions from left (red) to right (blue), and the slope decreases along the x direction (indicated with an arrow). Since a shift in the spectral/temporal phase corresponds to a shift in arrival time/center frequency, these plots indicate the presence of spatial chirp and pulse front tilt in the grating direction.

decreasing. In figure 5(c), the temporal phase plots show the slope of the temporal phase decreasing with x , which indicates a shift in center frequency as a function of transverse horizontal position.

To verify this cursory assessment, and to investigate the persistence of this behavior across all shots, the arrival time is extracted from the first order coefficient of the spectral phase fit for each shot (figure 5(a)), plotted, and fit to a polynomial (see figure 6, table 3). Along the x -direction (y -direction), the mean value of the arrival time across all positions and all shots was -8 ± 300 fs (210 ± 370 fs). An analogous temporal phase investigation for spatial chirp confirms its presence in the x and y domains as well. The center frequency is extracted from the first-order coefficient in the temporal phase (figure 5(b)), plotted and fit to a polynomial (see figure 6, table 3). Along the x -direction (y -direction), the mean value of the center frequency across all positions and all shots was $1.790 \text{ rad fs}^{-1} \pm 1.7 \times 10^{-4} \text{ rad fs}^{-1}$ ($1.789 \text{ rad fs}^{-1} \pm 3.2 \times 10^{-4} \text{ rad fs}^{-1}$).

Finally, the coefficient of determination R^2 is used to assess the proportion of variance in the data that is explained

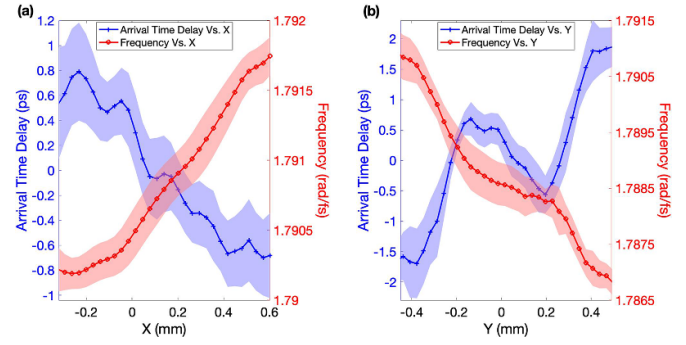


Figure 6. (a) Blue: arrival time across x , extracted from the spectral phase across x (see figure 5(a)) for all shots. Red: center frequency shift across x , extracted from the temporal phase across x (see figure 5(b)) for all shots. (b) Blue: arrival time across y , extracted from the spectral phase across y for all shots. Red: center frequency shift across y , extracted from the temporal phase across y for all shots. The mean value at each data point is plotted with error envelope indicating the shot-to-shot fluctuation in that value, quantified by the standard deviation over all shots at that location. All shots were taken on the same day. Across all shots, the pulse front tilt is roughly linear in the x direction (a) but shows a fifth order dependence in the y direction (b). The spatial dispersion is roughly linear in x with a weak quadratic term, while the data in y is best fitted by a fifth order polynomial (see table 1).

Table 3. Mean R -squared values by polynomial order of phase fit.

Order	Arrival time		Center freq. shift	
	x	y	x	y
1	0.79	0.64	0.90	0.94
2	0.81	0.66	0.97	0.95
3	0.85	0.78	0.98	0.97
4	0.88	0.80	0.99	0.97
5	0.90	0.92	0.99	0.99

by linear regression to a higher-order fit. Again, orders higher than fifth were not considered. Overall, in the horizontal direction, the arrival time shows a roughly linear dependence which fits to a cubic polynomial and the spatial dispersion shows a second-order polynomial dependence (see figure 6(a), table 3). A similar analysis for the vertical direction reveals a nonlinear arrival time dependence which is well fit by a fifth order polynomial, and the spatial dispersion fits to a fifth-order polynomial (see figure 6(b), table 3).

In addition to random shot-to-shot fluctuations, the systematic drift of key quantities—in particular, the arrival time and center frequency—over the course of the 22 consecutive maximum energy shots is studied. In order to investigate the change in the local arrival time τ relative to zero delay over the course of the shot day, τ is calculated for each location and for each shot. For each transverse position, the local change in arrival time between shots is estimated by linear regression and plotted (see figure 7(a)). The change in the local center frequency over the shot day is analogously derived. The local change in center frequency between shots

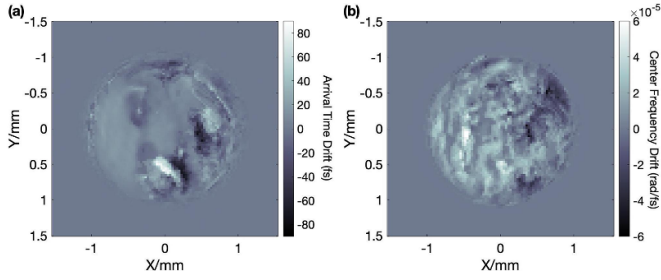


Figure 7. Drift over the course of the shot day in the arrival time (a) and center frequency (b).

is estimated by linear regression and plotted (see figure 7(b)). The mean drift in arrival time observed over all positions is 4 ± 20 fs, while the mean drift in center frequency is $7.2 \times 10^{-6} \text{ rad fs}^{-1} \pm 1.8 \times 10^{-5} \text{ rad fs}^{-1}$.

7. Single-shot movie and snapshot visualizations of a terawatt laser pulse

The complete retrieved electric field is a multidimensional, complex quantity that requires dynamic pulse propagation plots in order to effectively display all intensity and phase variations in space, time, and frequency. In order to present the full spatiotemporal field intuitively and meaningfully, we developed a 3D plotting method based on the pulse's spectrogram, where brightness indicates intensity and color represents the spectral energy distribution [45]. For color, RGB response functions $R(\omega)$, $G(\omega)$, and $B(\omega)$ are defined with centers at the low, center, and high frequencies within the pulse's spectrum, respectively, and normalized to the pulse spectrum, resulting in a white beam when all frequencies are present.

Dynamic color animations of a representative partial and full amplification shot are shown in visualizations 1 and 2, respectively. These movies depict the pulse's evolution on a femtosecond timescale at the STRIPED FISH measurement plane. The spatiotemporal distortions quantified in detail in previous sections can be seen in both movies. Pulse front tilt in both x and y is evident as the pulse moves diagonally across the screen, and spatial chirp is seen when the pulse is redder on the bottom left than on the top right. Similar motion and color are seen across both shots, which is consistent with the low variation in the pulse front tilt and spatial chirp extracted from the integrated intensity plots in figure 4.

To track the temporal motion of the pulse's hot spots, a 40% intensity threshold was applied to the movie frames. Although the spatiotemporal dependencies showed high consistency from shot to shot, the spatial profile had a higher number of hot spots after full amplification that were not present in the partially amplified pulse. The partially amplified shots had an average of 1.2 hot spots at a 40% intensity threshold, while the fully amplified shots had an average of 2.2 with values ranging from 1 to 4. Since no experimental conditions were changed between the two shot sets except for the charge state of the final amplifier rod, our conclusion is that this difference is attributable to variable gain across the final rod amplifier.

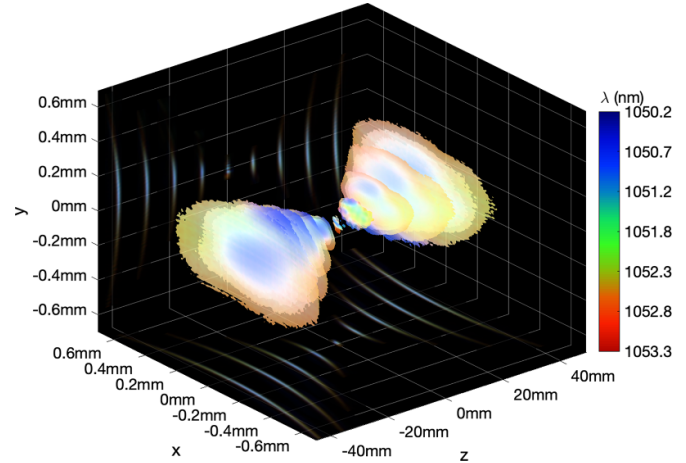


Figure 8. Pulse propagation plot of a single representative shot. The longitudinal propagation behavior was determined by calculating diffraction integrals [45]. Brightness indicates pulse intensity, and because the phase is responsible for the frequency distribution, the color distribution represents phase information. In this plot, we set $z = 0$ mm at the focus.

Next, the spatiotemporal electric field at the near-field STRIPED FISH measurement plane was numerically propagated into the far-field by calculation of angular-spectrum diffraction integrals [45],

$$E(k_x, k_y, \omega, z) = E(k_x, k_y, \omega, 0) \exp\left(iz\sqrt{\frac{\omega^2}{c^2} - k_x^2 - k_y^2}\right) \quad (3)$$

where $E(k_x, k_y, \omega, 0)$ is the 2D spatial Fourier transform of the retrieved electric field at the STRIPED FISH measurement plane, and k_x and k_y are the off-axis k -vectors in the x and y directions. We assume ideal achromatic focusing to obtain the electric field at the focus (see figure 8). The measured spatial phase was unwrapped along x , y , and t , and speckle noise was removed [58]. The angular dispersion varies with propagation [59], as do the pulse front tilt and spatial chirp [60, 61]. The spatially chirped focus is consistent with grating misalignment that can cause the pulse front tilt, spatial chirp, and angular dispersion that was observed at the STRIPED FISH measurement plane [51, 62]. Finally, the electric field evolution at a focus is plotted on a femtosecond timescale (see visualization 3), showing the persistence of the spatiotemporal distortions in the far-field.

8. Conclusion

The first single shot, complete spatiotemporal measurement of ultrashort pulses from an amplified laser system is reported on the COMET laser at Jupiter Laser Facility. Based on the analysis, laser compressor and stretcher alignment can be corrected by adjusting the positioning of the gratings to minimize angular dispersion. Misalignment in the laser compressor and stretcher is identified, along with higher-order spatiotemporal and spatio-spectral distortions. The single-shot nature of the STRIPED FISH measurement allows for a direct measurement of each shot, resulting in a statistical analysis of the beam's

stability. Numerical propagation of the STRIPED FISH measurement through the focal spot provides the first single shot, complete focal spot characterization of a terawatt laser system. We believe that such previously unavailable measurement capability will play a key role in optimizing all such high-intensity laser/amplifier systems, allowing the achievement of ever higher focal spot intensities and the study of increasingly-high-intensity exotic phenomena.

Data availability statement

The data that support the findings of this study are available upon reasonable request from the authors.

Funding

This work was completed under the auspices of the U.S. Department of Energy by Lawrence Livermore National Laboratory under contract DE-AC52-07NA27344 with funding support from the Laboratory Directed Research and Development Program under tracking code 17-ERD-039, and the DOE Office of Science Early Career Research Program under SCW1651. This work was supported in part by the National Science Foundation under Grant ECCS-1609808 and the Georgia Research Alliance.

Acknowledgments

This document was prepared as an account of work sponsored by an agency of the United States government. Neither the United States government nor Lawrence Livermore National Security, LLC, nor any of their employees makes any warranty, expressed or implied, or assumes any legal liability or responsibility for the accuracy, completeness, or usefulness of any information, apparatus, product, or process disclosed, or represents that its use would not infringe privately owned rights. Reference herein to any specific commercial product, process, or service by trade name, trademark, manufacturer, or otherwise does not necessarily constitute or imply its endorsement, recommendation, or favoring by the United States government or Lawrence Livermore National Security, LLC. The views and opinions of authors expressed herein do not necessarily state or reflect those of the United States government or Lawrence Livermore National Security, LLC, and shall not be used for advertising or product endorsement purposes.





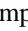
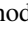




We acknowledge and thank the technical staff team at Jupiter Laser Facility for their assistance.

Conflict of interest

Rick Trebino discloses that he owns a company that sells pulse-measurement devices.

ORCID iDs

Elizabeth Grace  <https://orcid.org/0000-0003-4564-972X>

Tammy Ma  <https://orcid.org/0000-0002-6657-9604>
 Zhe Guang  <https://orcid.org/0000-0002-0500-8437>
 Rana Jafari  <https://orcid.org/0000-0001-7360-5527>
 Jaebum Park  <https://orcid.org/0000-0002-9108-4558>
 Gregory Kemp  <https://orcid.org/0000-0002-3825-3666>
 Michelle Rhodes  <https://orcid.org/0000-0003-3810-3737>
 Yuan Ping  <https://orcid.org/0000-0002-4879-9072>
 Ronnie Shepherd  <https://orcid.org/0000-0002-6697-2932>
 Brent Stuart  <https://orcid.org/0000-0003-2611-2046>
 Rick Trebino  <https://orcid.org/0000-0003-0661-0769>

References

- [1] Malinauskas M, Žukauskas A, Hasegawa S, Hayasaki Y, Mizeikis V, Buividas R and Juodkazis S 2016 Ultrafast laser processing of materials: from science to industry *Light. Sci. Appl.* **5** e16133
- [2] Froula D H, Turnbull D, Davies A S, Kessler T J, Haberberger D, Palastro J P, Bahk S-W, Begishev I A, Boni R, Bucht S, Katz J and Shaw J L 2018 Spatiotemporal control of laser intensity *Nat. Photon.* **12** 262
- [3] Chvykov V, Rousseau P, Reed S, Kalinchenko G and Yanovsky V 2006 Generation of 10^{11} contrast 50 TW laser pulses *Opt. Lett.* **31** 1456
- [4] Didenko N V, Konyashchenko A V, Lutsenko A P and Tenyakov S Yu 2008 Contrast degradation in a chirped-pulse amplifier due to generation of prepulses by postpulses *Opt. Express* **16** 3178
- [5] Akturk S, Gu X, Gabolde P and Trebino R 2005 The general theory of first-order spatio-temporal distortions of Gaussian pulses and beams *Opt. Express* **13** 8642
- [6] Akturk S, Gu X, Bowlan P and Trebino R 2010 Spatio-temporal couplings in ultrashort laser pulses *J. Opt.* **12** 093001
- [7] Pretzler G, Kasper A and Witte K J 2000 Angular chirp and tilted light pulses in CPA lasers *Appl. Phys. B* **70** 1
- [8] Isaienko O and Borguet E 2009 Pulse-front matching of ultrabroadband near-infrared noncollinear optical parametric amplified pulses *J. Opt. Soc. Am. B* **26** 965
- [9] Bromage J, Dorrer C and Zuegel J D 2010 Angular-dispersion-induced spatiotemporal aberrations in noncollinear optical parametric amplifiers *Opt. Lett.* **35** 2251
- [10] Zaukevičius A, Jukna V, Antipenkov R, Martinėnaitė V, Varanavičius A, Piskarskas A P and Valiulis G 2011 Manifestation of spatial chirp in femtosecond noncollinear optical parametric chirped-pulse amplifier *J. Opt. Soc. Am. B* **28** 2902
- [11] Giree A, Mero M, Arisholm G, Vrakking M J J and Furch F J 2017 Numerical study of spatiotemporal distortions in noncollinear optical parametric chirped-pulse amplifiers *Opt. Express* **25** 3104
- [12] Dunn J, Nilsen J, Osterheld A L, Li Y and Shlyaptsev V N 1999 Demonstration of transient gain x-ray lasers near 20nm for nickellike yttrium, zirconium, niobium, and molybdenum *Opt. Lett.* **24** 101
- [13] Stuart B C, Bonlie J D, Britten J A, Caird J A, Cross R R, Ebberts C A, Eckart M J, Erlandson A C, Molander W A, Ng A, Patel P K and Price D F *The Titan Laser at LLNL 2006 Conference on Lasers and Electro-Optics/Quantum Electronics and Laser Science Conference and Photonic Applications Systems Technologies, Technical Digest (CD)* (Long Beach, CA: Optical Society of America) p JTUG3 (<https://www.osapublishing.org/abstract.cfm?uri=QELS-2006-JTUG3>)

- [14] Miller G H, Moses E I and Wuest C R 2004 The National Ignition Facility *Opt. Eng.* **43** 2841
- [15] Rhodes M, Rahaman S, Bowlan P, Steinmeyer G and Trebino R 2014 From femtosecond to nanosecond, laser-pulse measurement is all about the single shot *Laser Focus World* **50** 97
- [16] Mangles S P D, Murphy C D, Najmudin Z, Thomas A G R, Collier J L, Dangor A E, Divall E J, Foster P S, Gallacher J G, Hooker C J, Jaroszynski D A, Langley A J, Mori W B, Norreys P A, Tsung F S, Viskup R, Walton B R and Krushelnick K 2004 Monoenergetic beams of relativistic electrons from intense laser-plasma interactions *Nature* **431** 535
- [17] O'Shea P, Kimmel M, Gu X and Trebino R 2001 Highly simplified device for ultrashort-pulse measurement *Opt. Lett.* **26** 932
- [18] Haefner C, Heebner J E, Dawson J, Fochs S, Shverdin M, Crane J K, Kanz K V, Halpin J, Phan H, Sigurdsson R, Brewer W, Britten J, Brunton G, Clark B, Messerly M J, Nissen J D, Shaw B, Hackel R, Hermann M, Tietbohl G, Siders C W and Barty C P J 2010 Performance measurements of the injection laser system configured for picosecond scale advanced radiographic capability *J. Phys. Conf. Ser.* **244** 032005
- [19] Cheng L, Banerjee S, Zhang J, Chen S, Brown K, Mills J, Powers N, Zhao B, Golovin G, Ghebregziabher I and Umstadter D 2013 Repetitive petawatt-class laser with near-diffraction-limited focal spot and transform-limited pulse duration *Proc. SPIE* **8599** 859919
- [20] Galletti M, Galimberti M and Giulietti D 2015 Ultra-short pulse reconstruction software in high power laser system *Nucl. Instrum. Methods Phys. Res. B* **355** 232
- [21] Hopps N, Oades K, Andrew J, Brown C, Cooper G, Danson C, Daykin S, Duffield S, Edwards R, Egan D, Elsmere S, Gales S, Girling M, Gumbrell E, Harvey E, Hillier D, Hoarty D, Horsfield C, James S, Leatherland A, Masoero S, Meadowcroft A, Norman M, Parker S, Rothman S, Rubery M, Treadwell P, Winter D and Bett T 2015 Comprehensive description of the Orion laser facility *Plasma Phys. Control. Fusion* **57** 064002
- [22] Galletti M, Galimberti M, Hooker C, Chekhlov O, Tang Y, Bisesto F G, Curcio A, Anania M P and Giulietti D 2016 An ultra short pulse reconstruction software applied to the GEMINI high power laser system *Nucl. Instrum. Methods Phys. Res. A* **829** 442
- [23] Nakamura K, Mao H, Gonsalves A J, Vincenti H, Mittelberger D E, Daniels J, Magana A, Toth C and Leemans W P 2017 Diagnostics, control and performance parameters for the BELLA high repetition rate petawatt class laser *IEEE J. Quantum. Electron.* **53** 1
- [24] Alessi D A, Prantil M A, Herriot S I, Hermann M R, Heebner J E, Williams W H, Lanier T, Widmayer C, Kalantar D H, Bowers M W, Pelz L J, Cabral J, Shaw M J, Di Nicola J G, Sigurdsson R, LaFortune K, Hamamoto M Y, Lawson J K, Lowe-Webb R R, Martinez D, Haefner C, Crane J K, Homoelle D, Barnes A, Paul M and Wegner P J 2020 High precision characterization of the kilojoule multi-ps Advanced Radiographic Capability *OSA High-brightness Sources and Light-driven Interactions Congress 2020 (EUVXRAY, HILAS, MICS)* ed L Assoufid and P Naulleau (Washington, DC: Optical Society of America) p HTh2B.5
- [25] Akturk S, Kimmel M, O'Shea P and Trebino R 2003 Measuring spatial chirp in ultrashort pulses using single-shot Frequency-Resolved Optical Gating *Opt. Express* **11** 68
- [26] Akturk S, Kimmel M, O'Shea P and Trebino R 2003 Measuring pulse-front tilt in ultrashort pulses using GRENOUILLE *Opt. Express* **11** 491
- [27] Rhodes M, Guang Z and Trebino R 2017 Unstable and Multiple Pulsing Can Be Invisible to Ultrashort Pulse Measurement Techniques *Appl. Sci.* **7** 40
- [28] Fuchs J, Antici P, d'Humières E, Lefebvre E, Borghesi M, Brambrink E, Cecchetti C A, Kaluza M, Malka V, Manclossi M, Meyroneinc S, Mora P, Schreiber J, Toncian T, Pépin H and Audebert P 2006 Laser-driven proton scaling laws and new paths towards energy increase *Nat. Phys.* **2** 48
- [29] Bowlan P, Gabolde P and Trebino R 2007 Directly measuring the spatio-temporal electric field of focusing ultrashort pulses *Opt. Express* **15** 10219
- [30] Bowlan P, Fuchs U, Trebino R and Zeitner U D 2008 Measuring the spatiotemporal electric field of tightly focused ultrashort pulses with sub-micron spatial resolution *Opt. Express* **16** 13663
- [31] Bowlan P, Gabolde P, Coughlan M A, Trebino R and Levis R J 2008 Measuring the spatiotemporal electric field of ultrashort pulses with high spatial and spectral resolution *J. Opt. Soc. Am. B* **25** A81
- [32] Bowlan P, Valtina-Lukner H, Löhmus M, Piksarv P, Saari P and Trebino R 2009 Measurement of the spatiotemporal electric field of ultrashort superluminal Bessel-X pulses *Opt. Photonics News* **20** 42
- [33] Saari P, Bowlan P, Valtina-Lukner H, Löhmus M, Piksarv P and Trebino R 2010 Basic diffraction phenomena in time domain *Opt. Express* **18** 11083
- [34] Bowlan P and Trebino R 2012 Using phase diversity for the measurement of the complete spatiotemporal electric field of ultrashort laser pulses *J. Opt. Soc. Am. B* **29** 244
- [35] Cohen J, Bowlan P and Trebino R 2012 Extending femtosecond metrology to longer, more complex laser pulses in time and space *IEEE J. Sel. Top. Quantum Electron.* **18** 218
- [36] Borot A and Quéré F 2018 Spatio-spectral metrology at focus of ultrashort lasers: a phase-retrieval approach *Opt. Express* **26** 26444
- [37] Jeandet A, Borot A, Nakamura K, Jolly S W, Gonsalves A J, Tóth C, Mao H-S, Leemans W P and Quéré F 2019 Spatio-temporal structure of a petawatt femtosecond laser beam *J. Phys. Photonics* **1** 035001
- [38] Gabolde P and Trebino R 2006 Single-shot measurement of the full spatio-temporal field of ultrashort pulses with multi-spectral digital holography *Opt. Express* **14** 11460
- [39] Gabolde P and Trebino R 2008 Single-frame measurement of the complete spatiotemporal intensity and phase of ultrashort laser pulses using wavelength-multiplexed digital holography *J. Opt. Soc. Am. B* **25** A25
- [40] Guang Z, Rhodes M, Davis M and Trebino R 2014 Complete characterization of a spatiotemporally complex pulse by an improved single-frame pulse-measurement technique *J. Opt. Soc. Am. B* **31** 2736
- [41] Guang Z, Rhodes M and Trebino R 2016 Measurement of the ultrafast lighthouse effect using a complete spatiotemporal pulse-characterization technique *J. Opt. Soc. Am. B* **33** 1955
- [42] Guang Z, Rhodes M, Trebino R et al 2017 Measuring spatiotemporal ultrafast field structures of pulses from multimode optical fibers *Appl. Opt.* **56** 3319
- [43] Zhu P, Jafari R, Jones T and Trebino R 2017 Complete measurement of spatiotemporally complex multi-spatial-mode ultrashort pulses from multimode optical fibers using delay-scanned wavelength-multiplexed holography *Opt. Express* **25** 24015
- [44] Guang Z, Rhodes M and Trebino R 2015 Numerical simulations of holographic spatio-spectral traces of spatiotemporally distorted ultrashort laser pulses *Appl. Opt.* **54** 6640

- [45] Rhodes M, Guang Z, Pease J and Trebino R 2017 Visualizing spatiotemporal pulse propagation: first-order spatiotemporal couplings in laser pulses *Appl. Opt.* **56** 3024
- [46] Jafari R and Trebino R 2018 High-speed “multi-grid” pulse-retrieval algorithm for frequency-resolved optical gating *Opt. Express* **26** 2643
- [47] Fittinghoff D N, DeLong K W, Trebino R and Ladera C L 1995 Noise sensitivity in frequency-resolved optical-gating measurements of ultrashort pulses *J. Opt. Soc. Am. B* **12** 1955
- [48] Bor Z, Racz B, Szabo G, Hilbert M and Hazim H A 1993 Femtosecond pulse front tilt caused by angular dispersion *Opt. Eng.* **32** 2501
- [49] Hebling J 1996 Derivation of the pulse front tilt caused by angular dispersion *Opt. Quantum Electron.* **28** 1759
- [50] Varjú K, Kovács A P, Kurdi G and Osvay K 2002 High-precision measurement of angular dispersion in a CPA laser *Appl. Phys. B* **74** s259
- [51] Osvay K, Kovacs A P, Heiner Z, Kurdi G, Klebiczki J and Csatari M 2004 Angular dispersion and temporal change of femtosecond pulses from misaligned pulse compressors *IEEE J. Sel. Top. Quantum Electron.* **10** 213
- [52] Osvay K, Kovács A P, Kurdi G, Heiner Z, Divall M, Klebiczki J and Ferincz I E 2005 Measurement of non-compensated angular dispersion and the subsequent temporal lengthening of femtosecond pulses in a CPA laser *Opt. Commun.* **248** 201
- [53] Gabolde P, Lee D, Akturk S and Trebino R 2007 Describing first-order spatio-temporal distortions in ultrashort pulses using normalized parameters *Opt. Express* **15** 242
- [54] Li D, Zeng S, Luo Q, Bowlan P, Chauhan V and Trebino R 2009 Propagation dependence of chirp in Gaussian pulses and beams due to angular dispersion *Opt. Lett.* **34** 962
- [55] Chauhan V, Cohen J and Trebino R 2010 Simple dispersion law for arbitrary sequences of dispersive optics *Appl. Opt.* **49** 6840
- [56] Nagelkerke N J D 1991 A note on a general definition of the coefficient of determination *Biometrika* **78** 691
- [57] Nabekawa Y and Midorikawa K 2003 High-order pulse front tilt caused by high-order angular dispersion *Opt. Express* **11** 3365
- [58] Xia H, Montresor S, Guo R, Li J, Yan F, Cheng H and Picart P 2016 Phase calibration unwrapping algorithm for phase data corrupted by strong decorrelation speckle noise *Opt. Express* **24** 28713
- [59] Varjú K, Kovács A P, Osvay K and Kurd G 2002 Angular dispersion of femtosecond pulses in a Gaussian beam *Opt. Lett.* **27** 2034
- [60] Martinez O E 1986 Grating and prism compressors in the case of finite beam size *J. Opt. Soc. Am. B* **3** 929
- [61] Martinez O E 1986 Pulse distortions in tilted pulse schemes for ultrashort pulses *Opt. Commun.* **59** 229
- [62] Greco M J, Block E, Meier A K, Beaman A, Cooper S, Iliev M, Squier J A and Durfee C G 2015 Spatial–spectral characterization of focused spatially chirped broadband laser beams *Appl. Opt.* **54** 9818